The Diverse Impacts of El Niño on Northeastern Canada and Greenland Surface Air Temperatures

RUYU GAN,[a,b] GANG HUANG,[b,c] AND KAIMING HU[b,d]

[a] *Ocean College, Jiangsu University of Science and Technology, Zhenjiang, China*
[b] *State key Laboratory of Numerical Modeling for Atmospheric Sciences and Geophysical Fluid Dynamics and Center for Monsoon System Research, Institute of Atmospheric Physics, Chinese Academy of Sciences, Beijing, China*
[c] *University of Chinese Academy of Sciences, Beijing, China*
[d] *Collaborative Innovation Center on Forecast and Evaluation of Meteorological Disasters (CIC-FEMD), Nanjing University of Information Science and Technology, Nanjing, China*

(Manuscript received 2 September 2022, in final form 3 October 2023, accepted 26 October 2023)

ABSTRACT: El Niño is known to affect Arctic temperature. However, the robustness of the observed relationship between El Niño and Arctic temperature remains debated. Here we reexamine the impacts of El Niño on the Arctic temperature in boreal winter [December–February (DJF)] using reanalysis datasets and atmospheric model experiments. This study shows that extreme El Niño events are accompanied by significant boreal winter cooling over northeastern Canada and Greenland (NECG), while moderate eastern Pacific (MEP) El Niño events are accompanied by significant boreal winter warming in this region. For central Pacific (CP) El Niño events, a cold signal appears in NECG, but with no statistical significance. During extreme El Niño winters, a positive Pacific–North America (PNA)-like pattern is seen in the Pacific, and anomalously negative 200-hPa geopotential height (Z200) strengthening occurs over NECG, which is a response to anomalous strong wave activity originating in the tropical Pacific. El Niño–induced circulation anomalies can further induce NECG cooling via cold temperature advection and decreased downward longwave radiation. In contrast, for the MEP El Niño, the subtropical jet extends zonally from the North Pacific to the North Atlantic, which is accompanied by increased baroclinicity anomalies and favors the propagation of synoptic eddies into the Atlantic, leading to a negative North Atlantic Oscillation (NAO)-like pattern. This in turn could further enhance the positive Z200 anomalies over NECG, resulting in anomalous warming in NECG through warm temperature advection and enhanced downward longwave radiation. A series of atmospheric model experiments simulates the observed circulation changes and associated warming over NECG.

SIGNIFICANCE STATEMENT: This work investigates the different impacts of the three El Niño types on regional Arctic wintertime temperature anomalies based on observations and model experiments. The impacts of El Niño events on northeastern Canada and Greenland temperatures during boreal winter show distinct differences between extreme El Niño and moderate EP El Niño events. These distinct differences can be attributed to the different atmospheric circulation patterns induced by different SST patterns, which can lead to warm (cold) temperature advection and enhanced (decreased) downward longwave radiation. These results highlight the different impacts of extreme and moderate EP El Niños on Arctic temperatures and provide an improved understanding of the impact of El Niños on the Arctic climate.

KEYWORDS: Atmosphere-ocean interaction; El Nino; Climate variability; Arctic

1. Introduction

The Arctic has experienced a secular warming trend in recent decades. Much attention has been given to Arctic warming because of its vital regional impacts and possible link to weather and climate at midlatitudes (Cohen et al. 2017, 2020; Dai and Song 2020; Screen et al. 2018; Shepherd et al. 2020). Arctic warming is most pronounced during boreal winter and is not spatially uniform (Bader 2014; Ding et al. 2014). The largest surface warming trend occurred in the Barents–Kara Seas (Bader 2014; Jung et al. 2017; Khan et al. 2014; Rantanen et al. 2022; Screen and Simmonds 2010). In addition to the Barents–Kara Seas, much attention has been given to warming in northeastern Canada and Greenland (NECG) because of its possible contribution to global sea level rise (Goelzer et al. 2020; Hofer et al. 2020; Meyssignac et al. 2017; Shepherd et al. 2020), weakening of the Atlantic meridional overturning circulation (Weijer et al. 2012), and associated changes in climate (Böning et al. 2016). Many possible mechanisms proposed to explain nonuniform Arctic warming can be loosely categorized into (i) local forcings and feedback (Dai et al. 2019; Kim and Kim 2019; Kim et al. 2019; Stuecker et al. 2018) and (ii) remote drivers (Screen et al. 2012; Yoshimori et al. 2017). The major remote drivers include poleward heat and moisture fluxes from tropical regions (Ding et al. 2014; Graversen and Burtu 2016; Graversen et al. 2008; McCrystall et al. 2020; Yoshimori et al. 2017), which can further enhance warming via local water vapor and cloud feedbacks (Francis and Hunter 2006; Ghatak and Miller 2013; Screen and Simmonds 2010; Serreze et al. 2012).

Corresponding authors: Gang Huang, hg@mail.iap.ac.cn; Kaiming Hu, hkm@mail.iap.ac.cn

DOI: 10.1175/JCLI-D-22-0677.1

Superimposed on the Arctic secular warming trend, Arctic temperature shows interannual variability that remains poorly understood. El Niño–Southern Oscillation (ENSO) is the most dominant mode in the tropical Pacific on an interannual time scale with well-known impacts on the global climate (Hoerling et al. 1997; Larkin 2005a,b; Rasmusson and Carpenter 1982; Trenberth 1997). There is growing evidence that the interannual variability in Arctic temperature fluctuations has been linked to ENSO variability, with El Niño contributing to anomalous cooling over the East Siberian Sea and La Niña having anomalous warming of the Kara Sea during boreal winter (Lee 2012).

ENSO events are known to vary in their location and intensity (An and Wang 2000; Ashok et al. 2007; Capotondi et al. 2015; Yeh et al. 2009), and different ENSO events can exert different climate impacts around the globe via large-scale atmospheric teleconnections (Garfinkel et al. 2019; King et al. 2018; Larkin 2005b; Yeh et al. 2009). Recent research on El Niño has classified El Niño events as eastern Pacific (EP) and central Pacific (CP) El Niño events based on the location of the maximum warming (Ashok et al. 2007; Fu and Fletcher 1985; Kao and Yu 2009; Kug et al. 2009; Yeh et al. 2009). Some studies have shown that the Arctic climate responses to EP El Niño events are different from those to CP El Niño events (Hu et al. 2016; Lee et al. 2023; Li et al. 2019; Matsumura et al. 2021). Li et al. (2019) found that EP El Niño events are usually accompanied by cooling in February over the Barents and Kara Seas, while CP El Niño events are usually accompanied by warming in February in northern Canada and Greenland. A recent study using models from phase 6 of the Coupled Model Intercomparison Project (CMIP6) provided climate modeling evidence and suggested distinctively different impacts of two types of El Niño events on Arctic winter (Lee et al. 2023). Matsumura et al. (2021) reported that summer Greenland warming is linked to central Pacific El Niño events. Hu et al. (2016) showed a linkage between the Arctic response over the Canada Basin and CP El Niño during boreal summer.

Whereas many previous studies have attempted to illustrate the link between different types of El Niño events and the Arctic climate (Hu et al. 2016; Jeong et al. 2022; Lee et al. 2023; Li et al. 2019), in many cases, the connection has been inferred from two types of El Niño events, which are classified as EP and CP El Niño events using ENSO indices. However, a slight difference in tropical Pacific convection during El Niño could result in differing teleconnection patterns and extratropical climate anomalies (Johnson and Kosaka 2016). Specifically, a recent study found that although both the 1982 and 1997 El Niño have been categorized as EP El Niño, they show distinctly different impacts on the pan-Arctic region due to differences in the eastern tropical Pacific SST (Jeong et al. 2022). Therefore, there is a need to examine the connection between Arctic temperature variation and individual El Niño events. Recently, El Niño events have been classified as extreme El Niño, moderate EP El Niño (MEP), and CP El Niño events using nonlinear *k*-means cluster analysis (Gan et al. 2023; Wang et al. 2019; Yang et al. 2021). Compared to the traditional EP–CP classification, this categorization distinguishes strong from moderate events (Wang et al. 2019). This nonlinear classification may help us to investigate the potential nonlinear linkage between Arctic temperature variation and individual El Niño events. The current study aims to investigate how these three types of El Niño events affect Arctic temperature to better understand the connection between El Niño and Arctic climate variability.

In the remainder of the paper, section 2 introduces the data and methods. In section 3, we display different Arctic temperature responses to three types of El Niño events. Section 4 will show the large-scale atmospheric teleconnection. The possible mechanisms and a series of general circulation model experiments are presented in section 5. A summary and discussion are presented in section 6.

2. Data and methods

a. Datasets

The monthly and daily-mean atmospheric reanalysis products for 2-m air temperature (T2m), 700-hPa air temperature (T700), 200-hPa geopotential height (Z200), 500-hPa geopotential height (Z500), 200-hPa wind, 250-hPa wind, 850-hPa wind, and downward infrared radiation (IR) are from the National Centers for Environmental Prediction (NCEP)–National Center for Atmospheric Research (NCAR) reanalysis-1 dataset (Kalnay et al. 1996). We also used the monthly and daily-mean atmospheric reanalysis from the fifth-generation ECMWF (ERA5) atmospheric reanalysis of the global climate (Hersbach et al. 2020). Observed monthly SST data were taken from the Extended Reconstructed Sea Surface Temperature version 5 global SST monthly dataset (ERSSTV5) (Huang et al. 2017). Our analyses focus on the period of 1950–2017. The long-term (1950–2017) mean and trend of all the daily or monthly data for each calendar day or month are removed.

We also used the NOAA-CIRES Twentieth Century Reanalysis (20CRv2c) (1871–2012) (Compo et al. 2011) and NCEP–NCAR reanalysis-1 dataset (1948–2020) (Kalnay et al. 1996) to make the "NCEP merged datasets." The two NCEP model datasets were combined into a merged NCEP reanalysis dataset using 20CRv2c (1880–1947) and the NCEP–NCAR reanalysis-1 dataset (1948–2017). To ensure temporal consistency, the differences in monthly climatology between the 20CRv2c and NCEP–NCAR reanalysis-1 datasets during the overlap period 1948–2012 were used to calibrate the mean state of NCEP–NCAR reanalysis-1. (The NCEP merged datasets from 1880 to 2017 were used for Figs. 2e–h.)

b. Methods

1) Definition of El Niño events

The relationship between winter Arctic temperature and different types of El Niño events is assessed for distinct El Niño events. Here we use extreme, MEP, and CP El Niño events following Wang et al. (2019). Extreme El Niño events commenced in the years 1972, 1982, 1997, and 2015. CP El Niño events commenced in the years 1986, 1991, 1994, 2002, 2004, 2006, 2009, and 2014. MEP El Niño events commenced in the years 1957, 1963, 1965, 1968, and 1976.

We acknowledge that the sample sizes of El Niño events are quite small. To examine the robustness of our result to the sample size of El Niño events, we also extend the record of El Niño events from 1950–2017 to 1880–2017. Following Gan et al. (2023), Extreme El Niño events commenced in the years 1888, 1902, 1972, 1982, 1997, and 2015; CP El Niño events commenced in the years 1885, 1896, 1930, 1986, 1991, 1994, 2002, 2004, 2006, 2009, and 2014; and MEP El Niño events commenced in the years 1899, 1904, 1911, 1913, 1919, 1923, 1925, 1951, 1957, 1963, 1965, 1968, and 1976. (Extended data from 1880 to 2017 were used for Figs. 2e–h. Figures 1 and 3–6 use the data from 1950 to 2017.)

2) WAVE-ACTIVITY FLUXES

The definition of the wave-activity fluxes follows Takaya and Nakamura (2001):

$$\mathbf{W} = \frac{1}{2|\mathbf{U}|}\begin{Bmatrix} \overline{u}(\psi_x'^2 - \psi'\psi_{xx}') + \overline{v}(\psi_x'\psi_y' - \psi'\psi_{xy}') \\ \overline{u}(\psi_x'\psi_y' - \psi'\psi_{xy}') + \overline{v}(\psi_y'^2 - \psi'\psi_{yy}') \\ \frac{f^2}{R\sigma/p}\left[\overline{u}(\psi_x'\psi_p' - \psi'\psi_{xp}') + \overline{v}(\psi_y'\psi_p' - \psi'\psi_{yp}')\right] \end{Bmatrix}. \tag{1}$$

Here, ψ denotes the streamfunction, f is the Coriolis parameter, R is the gas constant, $\mathbf{U} = (u, v)$ is the horizontal wind velocity, $\sigma = (R\overline{T}/C_p p) - d\overline{T}/dp$, with temperature T, and the specific heat at constant pressure C_p.

3) GEOPOTENTIAL TENDENCY

To investigate the interaction between transient eddies and the wave train, we used the quasigeostrophic geopotential tendency equation, Eliassen–Palm vectors and Eady growth rate.

The geopotential tendency at 250 hPa is used to study the effect of the downstream propagation of transient eddies on the geopotential. Following Lau and Holopainen (1984), it is given by

$$\left(\frac{\partial Z_{250}}{\partial t}\right)_{\text{eddy}} = \frac{f}{g}\nabla^{-2}\left[-\nabla\cdot(\overline{V'\zeta'})\right], \tag{2}$$

where f is the Coriolis parameter, g is the gravity constant, and ζ is the relative vorticity. Primes indicate high frequency and overbars indicate low frequency. Here we used bandpass frequencies between 2.5 and 7 days (primes) and low-pass frequencies of more than 30 days (overbars). The time filter is the same as that in Lau and Holopainen (1984).

4) ELIASSEN–PALM VECTORS

Eliassen–Palm vectors (hereafter referred to as E vectors) are used to illustrate the properties of transient eddies and local interactions between transient eddies and the time-mean flow (Hoskins et al. 1983). The horizontal components of **E** used in this study are given by Trenberth (1986)

$$\frac{1}{2}(\overline{v'^2} - \overline{u'^2})\mathbf{i} - \overline{v'u'}\mathbf{j}, \tag{3}$$

where u' and v' are the synoptic-scale daily 250-hPa winds subject to 2.5–7-day band filtering; the overbar represents the time average of a month; and **i** and **j** are the normal vectors in the zonal and meridional directions, respectively. The E vectors point approximately in the direction of the wave activity propagation relative to the local time-mean flow. The divergence and convergence of **E** indicate eddy-induced acceleration of the local mean zonal and meridional winds, respectively.

5) EADY GROWTH RATE

To explore the changes in baroclinicity and analyze its impact on the atmospheric circulation change, we calculated the maximum Eady growth rate (EGR) (Vallis 2017), which can be given by

$$\sigma_E = 0.3098\frac{|f|\left|\frac{\partial u}{\partial z}\right|}{N}, \tag{4}$$

where N is the Brunt–Väisälä frequency $N^2 = (g/\theta)(\partial\theta/\partial z)$, g is the acceleration due to gravity, θ is the potential temperature, and f is the Coriolis parameter.

6) TEMPERATURE TENDENCY BUDGET

The thermodynamic energy equation in pressure coordinates is calculated to study the budget of temperature tendency, including horizontal temperature advection and adiabatic warming. It is given by

$$0 = \frac{\partial T}{\partial t} = \gamma T = -\mathbf{V}_h\cdot\nabla_h T + S_p\omega + Q/C_p,$$

$$S_p = -\frac{T}{\theta}\frac{\partial\theta}{\partial p}, \tag{5}$$

where T is the temperature, t is the time, γ is the radiative relaxation time scale, $\mathbf{V}_h$ is the horizontal velocity vector, and ∇_h is the horizontal gradient operator; also, $-\nabla_h\cdot\nabla_h T$ is the horizonal temperature advection, S_p is a static stability parameter, θ is the potential temperature, p is the pressure, and ω is the vertical p velocity. The term $S_p\omega$ represents adiabatic warming (downward motion) or cooling (upward motion); Q represents the remaining diabatic heating contribution, including latent heating, infrared radiation (IR) warming by clouds, and surface heat fluxes; and C_p is the specific heat at constant pressure. We calculate the vertically integrated horizonal temperature advection and adiabatic warming/cooling from 1000 through 850 hPa to analyze the contribution of dynamic processes to account for the surface air temperature changes in the Arctic.

c. *ECHAM5 simulation*

We perform numerical experiments using the ECHAM5.4 atmospheric general circulation model (AGCM) developed by the Max Planck Institute (Roeckner et al. 2003). We used the T63L19 version, which has a triangular truncation at zonal wavenumber 63 (T63; equivalent to 1.98 horizontal resolution)

TABLE 1. Description of control and sensitivity experiments in ECHAM5.

Expt name	SST boundary condition
Control	Climatological SST over the global oceans for the period of 1979–96 with seasonal cycle
Extreme run	The composite extreme El Niño SST anomalies in the Pacific Ocean (40°S–50°N, 120°E–70°W) and in the Indian Ocean (20°S–20°N, 40°–100°E) are imposed
CP run	The composite CP El Niño SST anomalies in the Pacific Ocean (40°S–50°N, 120°E–70°W) are imposed
MEP run	The composite MEP El Niño SST anomalies in the Pacific and Atlantic Ocean (30°S–40°N, 120°E–0°) are imposed
MEP EP run	As in the MEP run, but with SST anomalies in the Pacific (30°S–40°N, 120°E–70°W)

and 19 sigma levels in the vertical. More information about this model can be found in Roeckner et al. (2003).

1) CONTROL SIMULATION

For the control simulation, the SST boundary conditions are composed of climatological SST and sea ice for the period of 1979–96 over the global oceans with a seasonal cycle.

2) SENSITIVITY EXPERIMENTS

To identify the SST pattern contributing to NECG cooling during the three types of El Niño events, three sets of sensitivity experiments (denoted extreme run, CP run, and MEP run) were conducted. For the extreme run, we first composite the DJF seasonal mean SST anomalies in extreme El Niño years. We then add SST anomalies over the Pacific (40°S–50°N, 120°E–70°W) and over the Indian Ocean (20°S–20°N, 40°–100°E) to climatological SST for December to February. Similarly, we composite the DJF SST anomalies over the Pacific (40°S–50°N, 120°E–70°W) in the CP El Niño years and then add them to climatological SST for December to February to force the CP run. For the MEP run, we added the composited DJF SST anomalies over the Pacific and Atlantic Oceans (30°S–50°N, 120°E–0°) of the MEP El Niño years to the climatological SST for December to February. In addition, to examine the impact of SST anomalies over the Atlantic on the extratropical climate during the winter of the MEP El Niño, we conducted one sensitivity experiment, with the composited DJF SST anomalies over the Pacific (30°S–40°N, 120°E–70°W) during the MEP El Niño winter added to the control run, referred to as the MEP EP run, and compared the difference between the MEP run and MEP EP run. Considering that the intensities of the MEP and CP El Niño events are weak, we doubled the SSTA for the MEP and CP El Niño events to enhance the atmospheric response. The above experiments are summarized in Table 1.

Each simulation (experiment) has 10 ensemble members. The simulations for each member were integrated for 14 months. The spinup period spans the first 11 months, and the last 3-month average (DJF) was taken as a sample. The 10 ensemble members

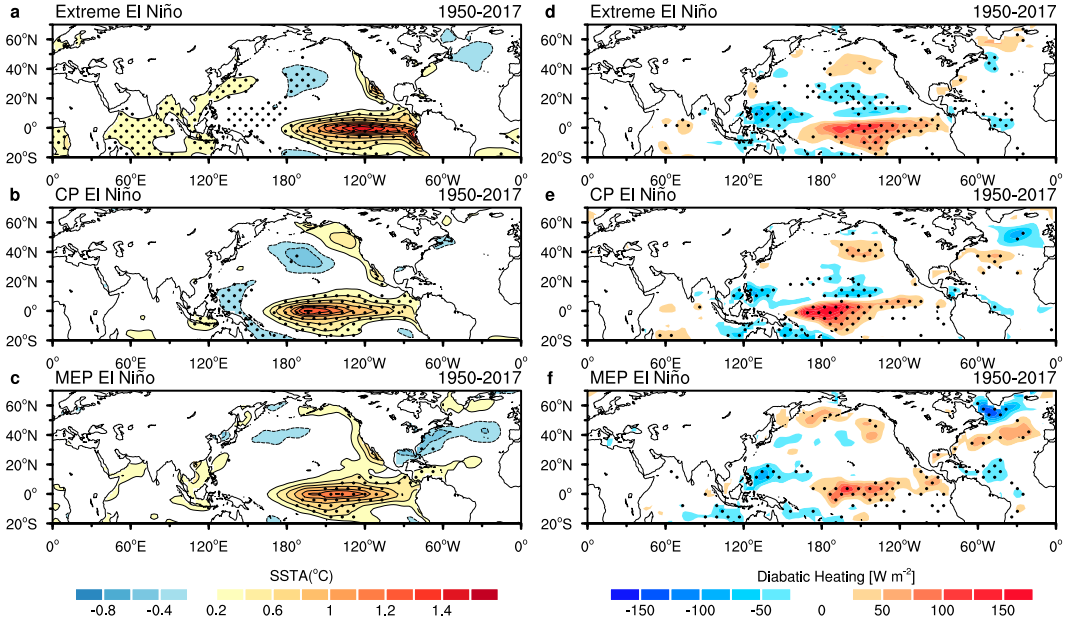

FIG. 1. (a)–(c) Composite of boreal winter (December–February) sea surface temperature anomalies (SSTA; shading; °C), which are normalized by the mean Niño-3.4 SST anomaly amplitude for (a) extreme El Niño, (b) CP El Niño, and (c) MEP El Niño events. (d)–(f) As in (a)–(c), but for diabatic heating anomalies (shading; W m^{-2}). The mean Niño-3.4 SST anomalies are 2.20°, 1.14°, and 1.03°C for extreme, MEP, and CP El Niño events, respectively. Stippling indicates that the composites are statistically significant at the 90% confidence level.

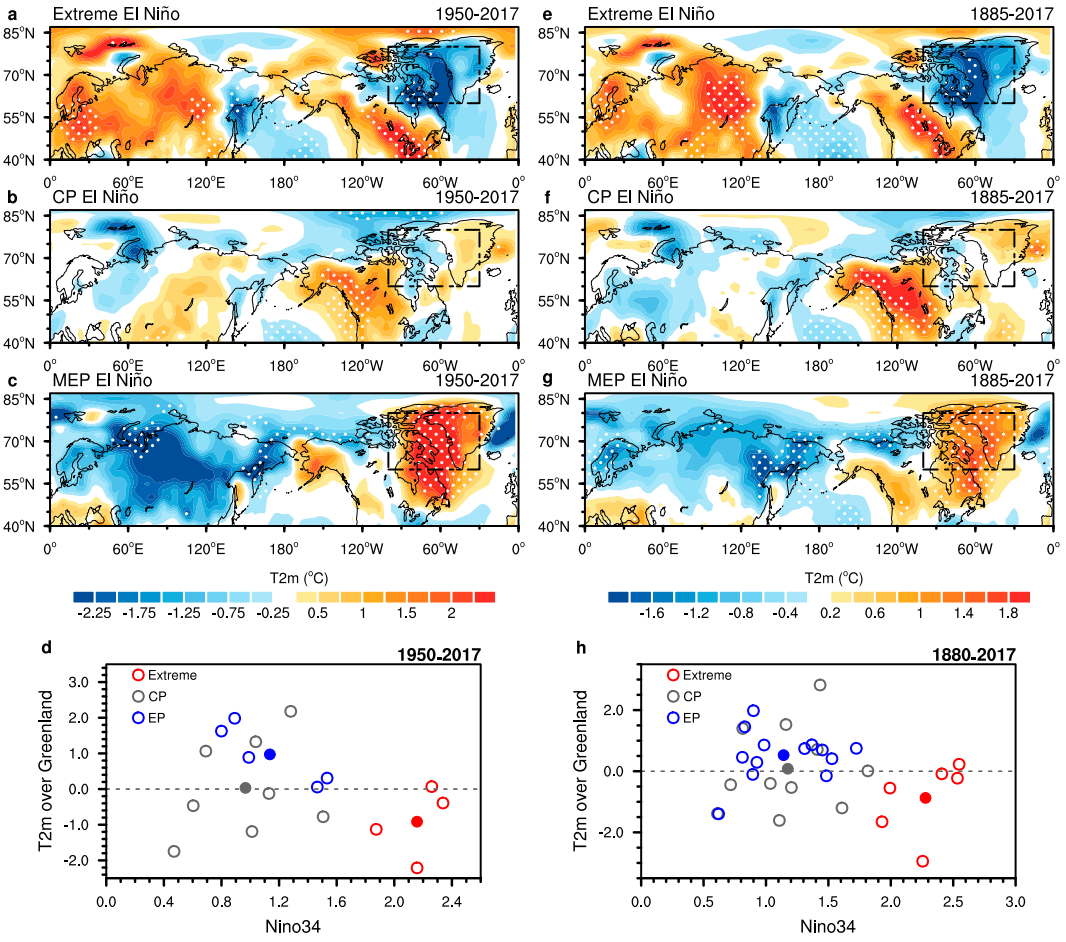

FIG. 2. (a)–(c) Composite of boreal winter (December–February) 2-m temperature anomalies (T2m; shading; °C) during (a) extreme El Niño, (b) CP El Niño, and (c) MEP El Niño. (e)–(g) As in (a)–(c), but extending the dataset to 1880–2017. Stippling indicates that the composites are statistically significant at the 90% confidence level. (d) Scatterplot between the standardized boreal winter (October–February) Niño-3.4 index (x axis; units: 1) and the averaged boreal winter (December–February) 2-m temperature anomalies over Greenland (60°–80°N, 100°–30°W), the black boxes in (a)–(c) regions (y axis; units: °C) among the three types of El Niño events. Red, gray, and blue hollow circles denote extreme El Niño, CP El Niño, and MEP El Niño events, respectively. Solid circles denote composites of different events. (h) As in (d), but extending the dataset to 1880–2017. In (e)–(h), the 2-m temperature datasets are derived from NOAA/NCEP. We made the "NCEP merged datasets" (1880–2017) by merging the NOAA-CIRES Twentieth Century Reanalysis (20CRv2c) from 1880 to 2012 and NCEP–NCAR reanalysis-1 data from 1948 to 2017.

were averaged to reduce the influence of internal variability. The anomalies are calculated from the differences between the sensitivity simulations and the control simulation.

3. Different Arctic temperature responses to the three types of El Niño events

Figures 1a–c show the composites of boreal winter large-scale SST anomalies induced by the extreme, MEP, and CP types of El Niño. During extreme El Niño boreal winter, strong anomalous warming is located in the eastern Pacific and tropical Indian Ocean (IO), while cold SST anomalies are shown in the tropical–extratropical Pacific (Fig. 1a). For CP El Niño events, the spatial pattern shows warm SST anomalies over CP, and cold SST anomalies appear in the tropical–extratropical WP (Fig. 1b). The maximum amplitude of CP El Niño is located at approximately 160°W. Compared with extreme El Niño events, the SST intensity is weaker, and the maximum center occurs more westward for CP El Niño events. Meanwhile, no significant warm SST anomalies occur in the tropical Indian Ocean. During the MEP El Niño boreal winter, the location of the center of maximum SST anomalies reaches approximately 140°W, which is approximately 20° west of the maximum center of extreme El Niño (Fig. 1c). This result is consistent with extreme El Niño events generally centered farther east (Capotondi et al. 2015; Takahashi et al. 2011). Compared to extreme El Niño and CP El Niño events, MEP El Niño events show significant cold SST anomalies in the Gulf of Mexico (Fig. 1c), leading to an enhanced SST gradient between tropical EP and the Gulf of Mexico. The different SSTA distributions are accompanied by large discrepancies in the

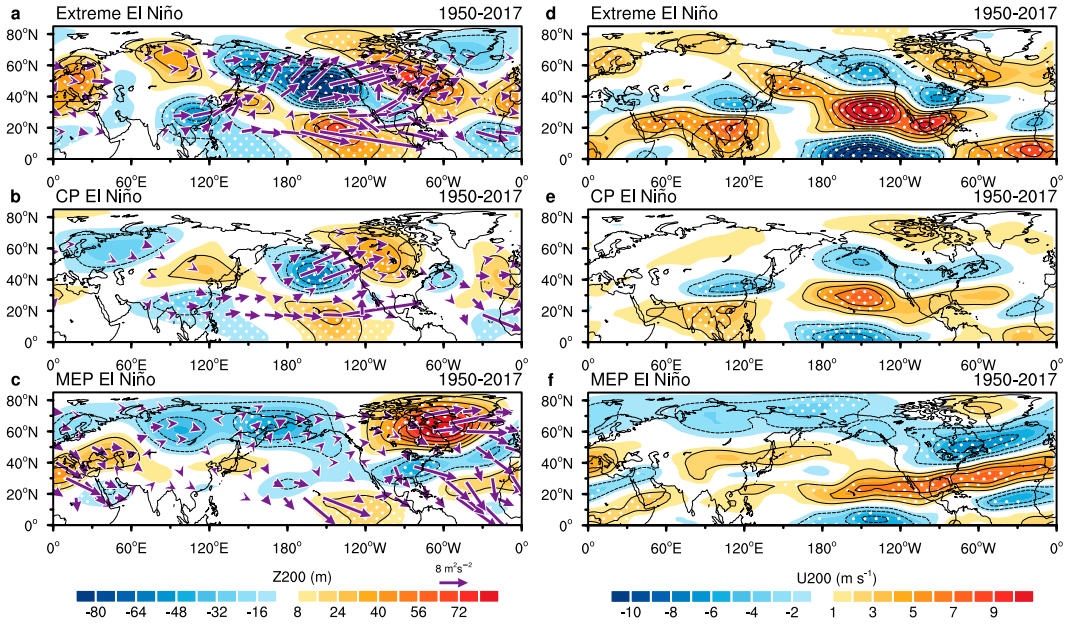

FIG. 3. Composite of nonzonal component of 200-hPa geopotential height (shading; m) and wave activity flux anomalies (vectors; $m^2\ s^{-2}$) in boreal winter (December–February) of (a) extreme El Niño, (b) CP El Niño, and (c) MEP El Niño. The wave activity flux anomalies are normalized by the mean Niño-3.4 SST anomaly amplitude. The mean Niño-3.4 SST anomalies are 2.20°, 1.14°, and 1.03°C for extreme, MEP, and CP El Niño events, respectively. Composite of 200-hPa zonal wind (shading; $m\ s^{-1}$) for (d) extreme El Niño, (e) CP El Niño, and (f) MEP El Niño winters. Stippling indicates the regions where the signal (group mean) is larger than noise (one standard deviation from the group mean of each member).

atmospheric convection changes in the tropics. Significant positive diabatic heating anomalies are located mainly over the equatorial eastern Pacific and central Pacific for extreme El Niño events (Fig. 1d), whereas they appear over the CP for CP El Niño events (Fig. 1e). For MEP El Niño events, the diabatic heating anomalies extend from the date line to the eastern equatorial Pacific and diabatic heating anomalies over EP are weaker than those of extreme El Niño events (Fig. 1f).

The diabatic heating pattern during El Niño can cause pronounced remote impacts on the global climate by exciting atmospheric wave teleconnections such as the Pacific–North American (PNA) teleconnection pattern (Gill 1980; Horel and Wallace 1981; Trenberth et al. 1998). We examined the 2-m temperature anomaly pattern during the boreal winter (averaged from December to February) of the three types of El Niño events. Statistically significant signals are found over northeastern Canada and Greenland (NECG; 60°–80°N, 100°–30°W) during the three types of El Niño boreal winters. Specifically, NECG was much colder than usual during the boreal winter of extreme El Niño events (Fig. 2a), whereas almost the opposite anomalies were evident over NECG during the boreal winter of MEP El Niño events (Fig. 2c). During the boreal winter of CP El Niño events, no statistically significant surface temperature signal is found over the NECG (Fig. 2b). To examine the NECG temperature responses to diverse El Niño types, we calculate temperature anomalies averaged over NECG for all three types of El Niño events. Extreme El Niño events are generally accompanied by cold winters, and MEP El Niño events are associated with warmer conditions (Fig. 2d). The mean response for extreme El Niño events is −0.92°C, while the mean response for MEP El Niño events is 0.97°C (Fig. 2d). We carried out sensitivity testing of our result to the sample size of El Niño events by extending the period to 1880–2017. The results still show that the Arctic boreal winter temperature responses to extreme and MEP El Niño events are different (Figs. 2e–h). Although interevent differences still exist for a particular type of El Niño event especially for CP El Niño events, a relatively large interevent consensus persists for extreme El Niño (5 out of 6; over 83%) and MEP El Niño events (10 out of 13; over 77%), providing some confidence in the result (Fig. 2h). Data uncertainties exist prior to 1979 in the polar region (Bromwich et al. 2007). To increase confidence in our results, we also used multiple datasets to examine the sensitivity of the results to different datasets (not shown). Although slight differences still exist, our key conclusion is not sensitive to the different datasets, and it provides some confidence in our results.

4. Large-scale atmospheric teleconnection

The different convective heating anomalies associated with the three types of El Niño events are accompanied by different atmospheric circulations. Figures 3a–c show the boreal winter nonzonal 200-hPa geopotential height (Z200) anomalies and wave activity flux for the three types of El Niño events in the Northern Hemisphere. For extreme and CP

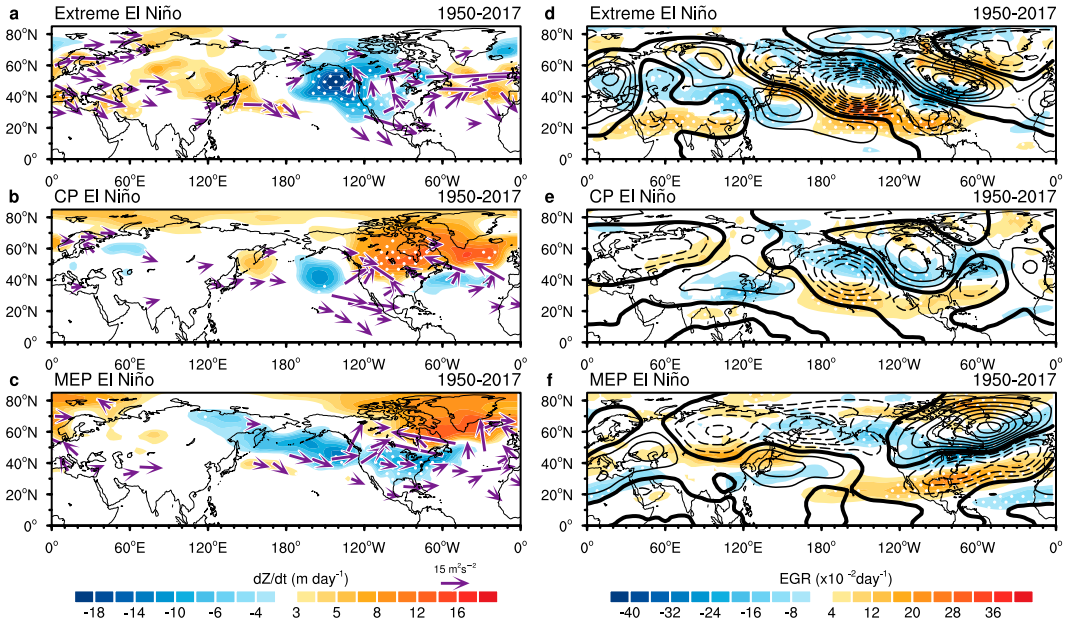

FIG. 4. Composites of boreal winter (December–February) 250-hPa geopotential height tendency forced by transient eddies (shading; m day^{-1}) and 250-mb Eliassen–Palm E vectors (vectors; m^2 s^{-2}) for (a) extreme El Niño, (b) CP El Niño, and (c) MEP El Niño. Composite of boreal winter (December–February) vertically integrated EGR from 1000 to 300 hPa (shading; 10^{-2} day^{-1}) and 500-hPa geopotential height anomalies (contours; m) during (d) extreme El Niño, (c) CP El Niño, and (f) MEP El Niño. Stippling indicates the regions where the signal (group mean) is larger than noise (one standard deviation from the group mean of each member). The E vectors with magnitudes smaller than 7 m^2 s^{-2} are not plotted.

El Niño events, the Z200 pattern shows an anomalously negative Z200 over NECG and a positive PNA-like pattern with positive Z200 anomalies over the tropical EP and northwest United States and negative Z200 anomalies over the North Pacific (Figs. 3a,b). The wave activity fluxes show anomalously strong wave activity originating in the tropical Pacific and extending northeastward from the central tropical Pacific toward NECG (Figs. 3a,b). For MEP El Niño events, the PNA pattern is different from that of the extreme and CP El Niño events, with prominent positive Z200 anomalies over NECG and negative Z200 anomalies over the southern United States and the extratropical Atlantic Ocean (Fig. 3c). The negative Z200 anomalies over the extratropical Atlantic Ocean and positive Z200 anomalies over NECG resemble the negative phase of the NAO. The corresponding flux of wave activity increases over NECG. Figures 3d–f show the composite of 200-hPa zonal wind (U200) anomalies during the three types of El Niño events. The most notable feature of zonal wind anomalies during the MEP El Niño events, compared to the extreme and CP El Niño events, was an anomalous STJ extending zonally from the EP to NA and a weakened Atlantic jet (Fig. 3f). The eastward elongation of the subtropical jet could affect the propagation of tropical-induced planetary waves (Ambrizzi and Hoskins 1997; Jiménez-Esteve and Domeisen 2018; Li and Lau 2012; Graf and Zanchettin 2012). For the MEP El Niño events, the anomalous wave activity originating in the tropical Pacific is weaker than that of extreme and CP El Niño events (Fig. 3c).

Why does the STJ extend zonally only in the boreal winter of the MEP El Niño but not in the extreme El Niño and CP El Niño events? During the boreal winter of MEP El Niño events, significant SST warming in the central and eastern equatorial Pacific and SST cooling in the Gulf of Mexico and North Atlantic (Fig. 1c) cause an increase in the temperature gradient in the eastern Pacific and North Atlantic at approximately 30°N, which could result in enhanced subtropical baroclinicity over the eastern Pacific and North Atlantic (Fig. 4f). The enhanced subtropical baroclinicity over the eastern Pacific and North Atlantic could reinforce the eastward extension of eddy activity (Fig. 4c), which could be a possible explanation for the zonal extension of the STJ from the North Pacific to the North Atlantic (Li and Lau 2012). However, for extreme and CP El Niño events, there is no significant SST cooling in the Gulf of Mexico and North Atlantic (Figs. 1a,b). Correspondingly, the enhanced meridional temperature gradient and enhanced subtropical baroclinicity mainly occur in the eastern Pacific at approximately 30°N and do not extend into the Atlantic (Figs. 4d–f); thus, an eastward-extended STJ does not appear in extreme El Niño and CP El Niño events (Figs. 3d–f).

5. Possible mechanisms for different Arctic SAT responses to the three El Niño types

Dynamic processes (i.e., horizontal temperature advection and vertical adiabatic processes) or moisture transport and

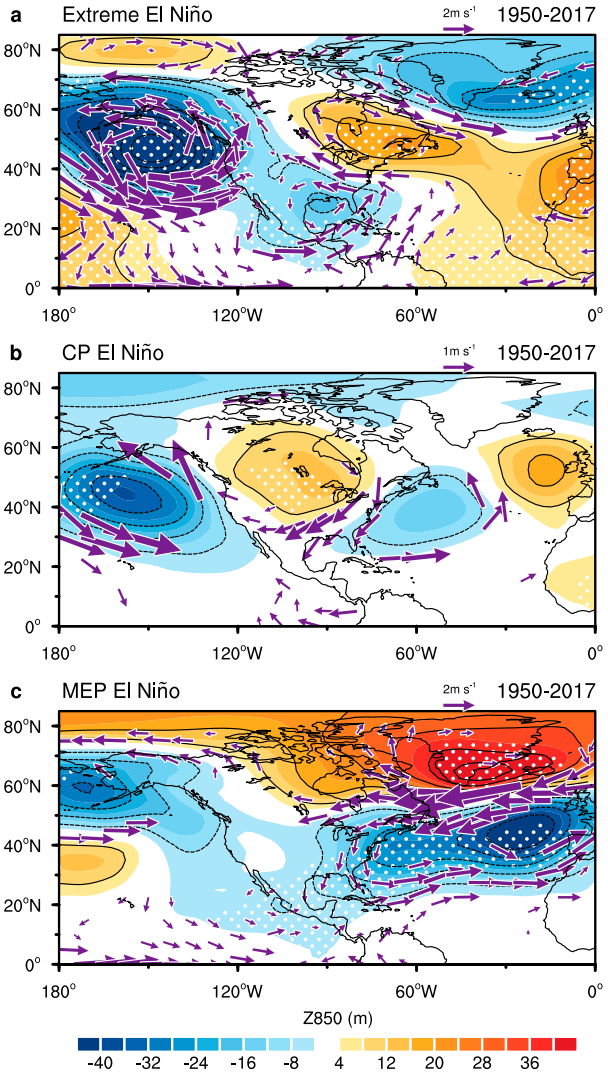

FIG. 5. Composite of 850-hPa geopotential height (shading; m) and 850-hPa wind anomalies (vectors; m s^{-1}) in boreal winter (December–February) of (a) extreme El Niño, (b) CP El Niño, and (c) MEP El Niño events. Stippling indicates the regions where the 850-hPa geopotential height signal (group mean) is larger than noise (one standard deviation from the group mean of each member).

subsequent changes in cloudiness and downward longwave radiation are identified as potential candidates for Arctic temperature variability (Ding et al. 2014; He et al. 2020; Park et al. 2018). To examine the role of dynamic processes and downward infrared radiation (IR), we show the atmospheric circulation and calculate the lower-tropospheric (1000–850 hPa) heat budget for the three types of El Niño events.

For extreme El Niño events, the anomalous 850-hPa geopotential height pattern shows significant negative values in the NECG and positive values in northwestern North America, leading to dominant northwesterly wind anomalies in the southwestern part of the NECG (Fig. 5a). These northwesterly wind anomalies bring relatively colder air into the NECG, with cold temperature advection evident over the NECG (Fig. 6a). For MEP El Niño events, the anomalous 850-hPa geopotential height pattern exhibits positive values in NECG, which is associated with anticyclonic circulation dominating in this region (Fig. 5c), resulting in warm temperature advection (Fig. 6c). For adiabatic processes, however, the contribution of adiabatic warming/cooling is less significant overall, although there is slight adiabatic warming during the extreme (Fig. 6d) and slight adiabatic cooling during the EP El Niño (Fig. 6f).

In addition to dynamic processes, warming or cooling in the Arctic could be linked to moisture transport and subsequent changes in downward longwave radiation. Since the surface temperature is tightly coupled to downward longwave radiation (Vargas Zeppetello et al. 2019), we do not attempt to distinguish the cause and effect between the two. For extreme El Niños, the cooling of the surface over the NECG is accompanied by negative local downward longwave radiation anomalies (Fig. 6g). The deceased downward longwave radiation anomalies could further reinforce the cooling here. In contrast, for the MEP El Niño, the NECG surface warming is accompanied by positive local downward longwave radiation (Fig. 6i). The enhanced downward longwave radiation over NECG could further favor warming here. Based on the lower-tropospheric (1000–850-hPa) heat budget, for extreme and MEP El Niños, the Greenland SAT pattern can be largely linked to downward longwave radiation (Fig. 6j). The horizontal temperature advection partly explains the Greenland SAT pattern. This result is consistent with previous studies that argued that Arctic SAT changes could be primarily linked to downward longwave radiation (Jeong et al. 2022; Park et al. 2015). The contribution of adiabatic processes is much smaller than the contributions of horizontal temperature advection and downward longwave radiation.

To further verify whether the observed Arctic temperature responses to SST anomalies associated with different El Niño types can be simulated (experiments described in section 2c), a series of numerical simulations are performed using ECHAM5, which is an AGCM from the Max Planck Institute (Roeckner et al. 2003).

Figures 7 and 8 show the simulated ensemble-mean winter Arctic temperature anomalies and large-scale teleconnections for the extreme run, CP run, and MEP run experiments. For the extreme run, negative temperature anomalies are simulated over the NECG, which is largely consistent with the observations (Fig. 7a). The simulated Z200 response to the extreme run shows negative values over the NECG and positive Z200 anomalies over the tropical EP and northwest United States and negative Z200 anomalies over the North Pacific and southern United States (Fig. 8a), suggesting that the model is capable of reproducing the deepening of the low over Greenland and the positive PNA-like pattern.

For the CP run, the model simulated cold anomalies and negative geopotential height anomalies over the NECG. For the MEP run, ECHAM5 reproduced the observed strong ridge and warm temperature anomalies over the NECG well. However, the simulation fails to reproduce the observed cooling over the Eurasian continent during MEP El Niño winters (Fig. 7c). It is noteworthy that in the CP run and MEP run,

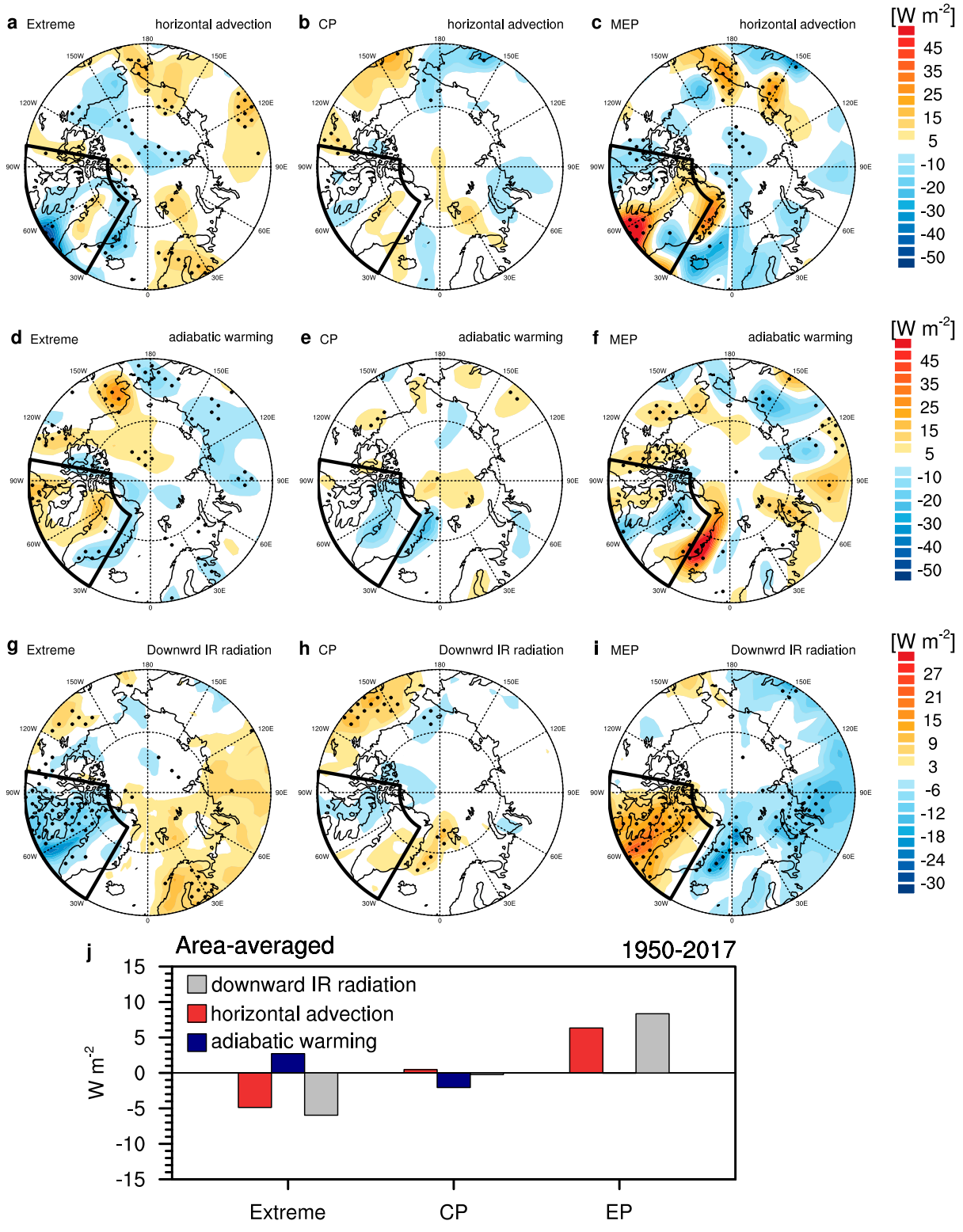

FIG. 6. Composite of anomalous (a)–(c) vertically integrated horizontal temperature advection (shading; W m^{-2}) and (d)–(f) adiabatic warming (shading; W m^{-2}) from 1000 through 850 hPa during winter (DJF) of (left) extreme El Niño, (center) CP El Niño, and (right) MEP El Niño. (g)–(i) As in (a)–(c), but for downward infrared radiation (IR; W m^{-2}). (j) Average anomalous vertically integrated horizontal temperature advection (W m^{-2}) and vertically integrated adiabatic warming (W m^{-2}) and downward IR (W m^{-2}) over the Greenland (60°–80°N, 100°–30°W) regions for extreme El Niño, CP El Niño, and MEP El Niño events. Stippling indicates the regions where the signal (group mean) is larger than noise (one standard deviation from the group mean of each member).

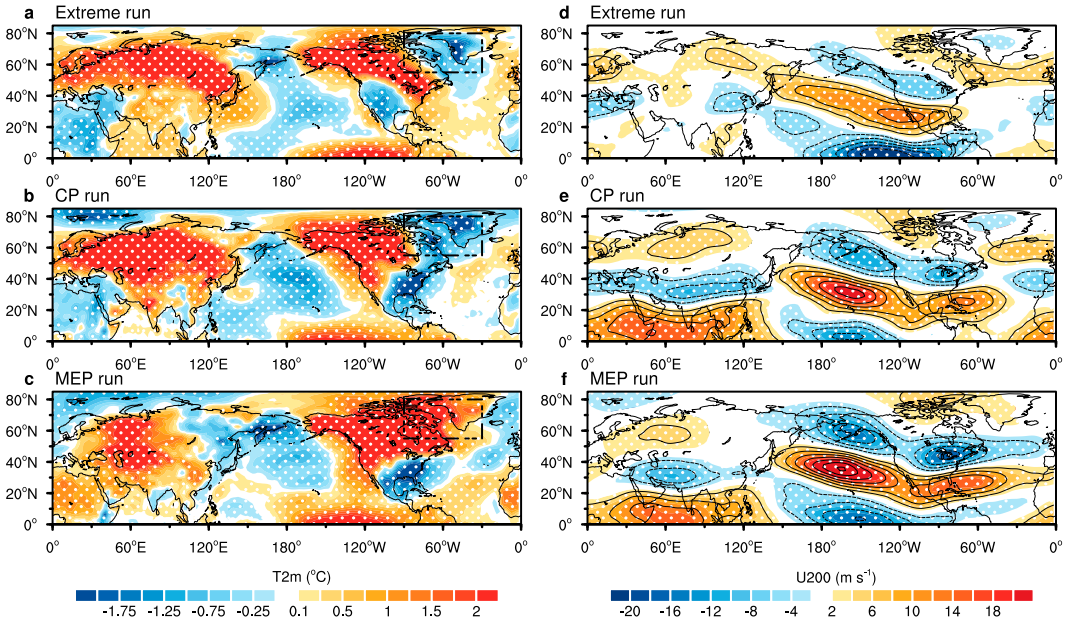

FIG. 7. Simulated ensemble mean winter (DJF) (a)–(c) 2-m temperature (shading; °C) and (d)–(f) 200-hPa zonal wind (shading; m s^{-1}) responses regarding a difference between the (top) extreme run and control run, (middle) CP run and control run, and (bottom) MEP run and control run. Stippling indicates the regions where the signal (group mean) is larger than noise (one standard deviation from the group mean of each member).

the location of the simulated positive geopotential height anomalies over the Eurasian continent differs from the observations, with more eastward extension in the simulation. This result suggests that the model utilized here has a poor performance on the Eurasian continent. Considering that the observed composite surface temperature anomalies over the Eurasian continent are not statistically significant for CP and MEP El Niños, this result also suggests that other factors may be linked to the temperature changes over the Eurasian continent. Although the ECHAM5 results do not match the observational results completely, especially in the Eurasian continent, the model results quite realistically reproduced the features of observed temperature and geopotential height anomalies over North America and Greenland during extreme, MEP, and CP El Niño winters, respectively, including the negative (positive) temperature and geopotential height anomalies over the NECG during extreme (MEP) El Niño winter. The simulated 200-hPa wind anomalies are also similar to those in the observations (Figs. 7d–f). The model simulated eastward elongation of the subtropical jet from the EP to NA for MEP El Niño events. In contrast, the extreme run and CP run induce a tripolar structure of the subtropical jet over the NP but no eastward elongation from the EP to NA (Figs. 7d,e). Thus, the simulated results suggest that the different temperature and atmospheric responses in the Arctic region during the boreal winter of the three El Niño types can be viewed as responses to the imposed SST anomalies related to the three El Niño types.

We note that there are anomalously cold SST anomalies over the Atlantic and warm SST anomalies over the Pacific during the winter of MEP El Niño. To further examine the impact of SST anomalies over the Atlantic on extratropical climate during the winter of the MEP El Niño, we performed one sensitivity experiment in which composited SST anomalies over the Pacific (referred to as the MEP EP run) were imposed and compared the differences between the response to the MEP run and MEP EP run. Compared to the MEP EP run, the MEP run shows enhanced warming over NECG, indicating that the SST anomalies over the North Atlantic Ocean (NA) could enhance warming over NECG (Fig. 9). Meanwhile, the positive anomalies over the high latitudes of NA and negative anomalies over central NA are much larger in the MEP run than in the MEP EP run, which resembles a negative NAO-like pattern. Previous studies showed that warm SST anomalies in the eastern equatorial Pacific and cold SST anomalies in the Gulf of Mexico and North Atlantic Ocean could enhance the subtropical baroclinicity over the eastern tropical Pacific, which favors the shift of the Pacific jet and is conducive to the eastward propagation of transient eddies into the Atlantic, thus resulting in a negative NAO-like pattern (Jiménez-Esteve and Domeisen 2018; Li and Lau 2012). Therefore, we suspect that the significant NECG cooling during the MEP winter is maintained by a combined effect of EP warming and NA cooling.

6. Summary and discussion

We have investigated the different responses of NECG temperature to three different types of El Niño events using reanalysis datasets and model experiments.

A stable relationship is found between the three types of El Niño events and temperature anomalies in the NECG.

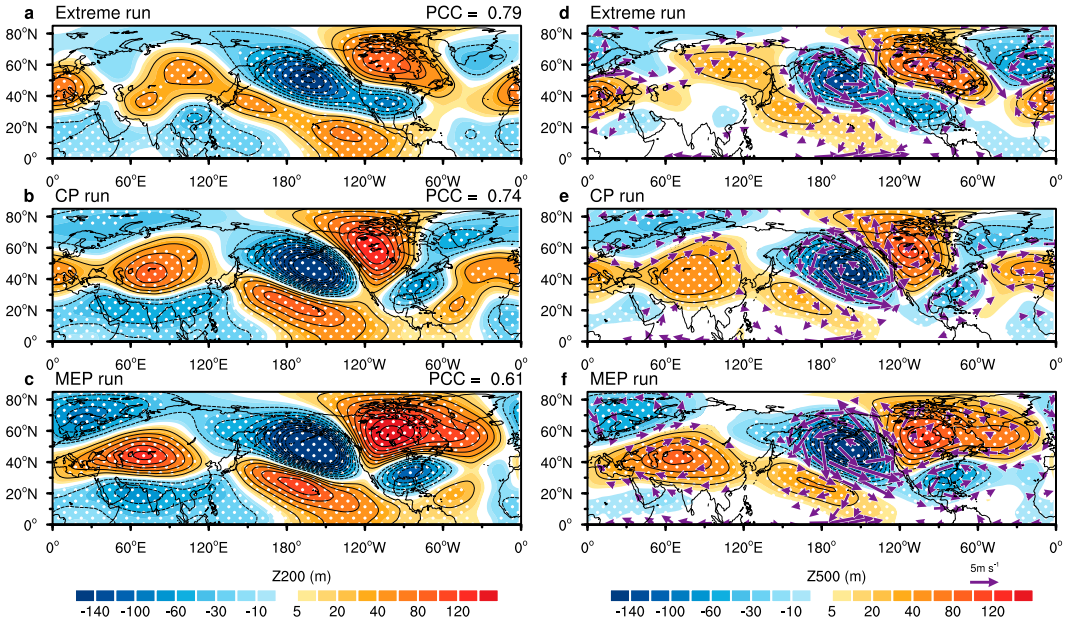

FIG. 8. Simulated ensemble mean winter (DJF) (a)–(c) Z200 (shading; m) and (d)–(f) Z500 (shading; m) and 850-hPa wind anomaly (vectors; m s^{-1}) responses regarding a difference between the (top) extreme run and control run, (middle) CP run and control run, and (bottom) MEP run and control run. Stippling indicates the regions where the signal (group mean) is larger than noise (one standard deviation from the group mean of each member). The pattern correlation coefficients between the observed (Figs. 3a–c) and ECHAM5 simulated ensemble-mean nonzonal Z200 anomalies (Figs. 8a–c) in the Northern Hemisphere (0°–90°N) are 0.79, 0.74, and 0.61 for extreme, CP, and MEP El Niño events, respectively.

Specifically, statistically significant cooling temperature anomalies are found over NECG during boreal winters of extreme El Niño events, while statistically significant warming signals are evident over NECG during boreal winters of MEP El Niño events. For CP El Niño events, there is no statistically significant surface temperature signal over the NECG. Quantitatively, the mean response of the temperature anomalies over NECG for extreme El Niño events is −0.92°C, while the mean response for MEP El Niño events is 0.97°C. Note that our results are not inconsistent with previous studies that defined EP El Niño events using the ENSO index and found that EP El Niño events generate no statistically significant signal over the NECG regions (Li et al. 2019). The view of the EP El Niño impact on NECG regions in Li et al. (2019) may be a mixture of the different impacts from extreme El Niño and moderate EP El Niño events. The distinctly different impacts of extreme El Niño and moderate EP El Niño on NECG temperatures suggest that EP El Niño events need to distinguish strong from moderate events to better understand the impacts of El Niño on the Arctic climate.

This study has further shown that the different kinds of El Niño events could generate different tropics-to-Arctic teleconnection patterns due to the different SST patterns. During extreme El Niño winters, the Z200 anomalies show significant negative geopotential height anomalies over northeastern Canada and a positive PNA-like pattern, which is associated with strong wave activity originating in the tropical Pacific and extending into the Arctic. During the MEP El Niño winter, the Z200 anomalies show statistically significant positive geopotential height anomalies over northeastern Canada and a negative NAO-like pattern over the NA region, with eastward elongation of the subtropical jet from the EP to NA.

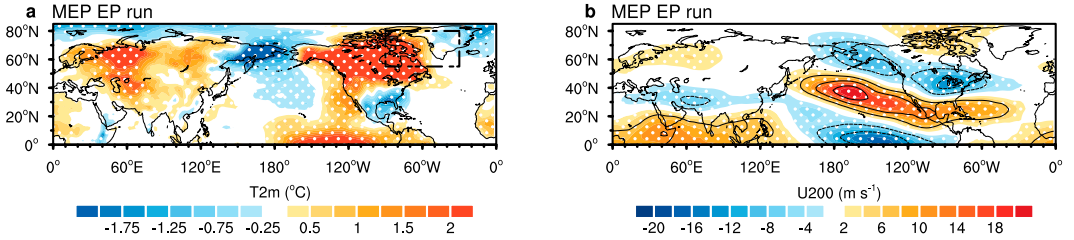

FIG. 9. As in Fig. 7, but for the MEP EP run. Stippling indicates the regions where the signal (group mean) is larger than noise (one standard deviation from the group mean of each member).

The different tropics-to-Arctic teleconnection patterns likely contribute to the different Arctic temperature anomalies via dynamic processes and moisture transport. For extreme El Niños, strong cold temperature advection and decreased downward longwave radiation could be found over NECG, leading to cooling here. For MEP El Niño events, warm temperature advection and enhanced downward longwave radiation are dominant over NECG, leading to warmer than normal temperatures. The numerical simulations forced by the observed El Niño SST anomaly reproduced the observed features in NECG, including wintertime temperature change and large-scale atmospheric circulation.

The major finding in this study is the distinct different winter NECG temperature responses to extreme El Niño and MEP El Niño events. Due to the lack of consistency in the response of the NECG to CP El Niño events in the observations, we do not emphasize CP El Niño events in this study. There are some limitations in this study. First, although extending datasets to 1880, the number of El Niño samples in the observations is still limited. In particular, all the MEP El Niño events occurred prior to 1976, and it is difficult to exclude decadal modulation in the observations. For example, it is possible that the MEP El Niño–related teleconnection and its climate impact are modulated by decadal climate variability (e.g., NAO). Further deeper understanding of the impact of MEP El Niño on Arctic temperature is still needed. Additionally, probably due to the limited samples, the statistical significance of our results is limited, with a 90% confidence level. Some recent studies used large climate model outputs to overcome the shortfall of samples in observations (e.g., Clancy et al. 2021; Lee et al. 2023). Therefore, in future work, the relationship between the three types of El Niño and Arctic winter temperature should be further examined by using model large ensembles. Some recent studies (e.g., Jeong et al. 2022) suggested that the Indian Ocean SST anomalies can effectively impact Arctic winter temperature. For instance, Jeong et al. (2022) showed that warm Indian Ocean SST anomalies could favor Arctic winter warm anomalies. For MEP El Niño events, however, the warm SST anomalies are not obvious. Thus, the role of the Indian Ocean is not emphasized in this study.

Acknowledgments. This work was supported by the National Natural Science Foundation of China (42141019, 41831175, 42175040, 91937302, and 41721004), the Second Tibetan Plateau Scientific Expedition and Research Program (2019QZKK0102) and Youth Innovation Promotion Association of CAS (2021072).

Data availability statement. All the data in this paper are publicly available from the following websites: ERSST, available at https://www.ncei.noaa.gov/products/extended-reconstructed-sst; the NCAR reanalysis-1 dataset from https://psl.noaa.gov/data/gridded/data.ncep.reanalysis.html; the ERA5 dataset from https://climate.copernicus.eu/climate-reanalysis; and the 20CRv2c dataset from https://climatedataguide.ucar.edu/climate-data/noaa-20th-century-reanalysis-version-2-and-2c.

REFERENCES

Ambrizzi, T., and B. J. Hoskins, 1997: Stationary Rossby-wave propagation in a baroclinic atmosphere. *Quart. J. Roy. Meteor. Soc.*, **123**, 919–928, https://doi.org/10.1002/qj.49712354007.

An, S.-I., and B. Wang, 2000: Interdecadal change of the structure of the ENSO mode and its impact on the ENSO frequency. *J. Climate*, **13**, 2044–2055, https://doi.org/10.1175/1520-0442(2000)013<2044:ICOTSO>2.0.CO;2.

Ashok, K., S. K. Behera, S. A. Rao, H. Weng, and T. Yamagata, 2007: El Niño Modoki and its possible teleconnection. *J. Geophys. Res.*, **112**, C11007, https://doi.org/10.1029/2006JC003798.

Bader, J., 2014: The origin of regional Arctic warming. *Nature*, **509**, 167–168, https://doi.org/10.1038/509167a.

Böning, C. W., E. Behrens, A. Biastoch, K. Getzlaff, and J. L. Bamber, 2016: Emerging impact of Greenland meltwater on deepwater formation in the North Atlantic Ocean. *Nat. Geosci.*, **9**, 523–527, https://doi.org/10.1038/ngeo2740.

Bromwich, D. H., R. L. Fogt, K. I. Hodges, and J. E. Walsh, 2007: A tropospheric assessment of the ERA-40, NCEP, and JRA-25 global reanalyses in the polar regions. *J. Geophys. Res.*, **112**, D10111, https://doi.org/10.1029/2006JD007859.

Capotondi, A., and Coauthors, 2015: Understanding ENSO diversity. *Bull. Amer. Meteor. Soc.*, **96**, 921–938, https://doi.org/10.1175/BAMS-D-13-00117.1.

Clancy, R., C. Bitz, and E. Blanchard-Wrigglesworth, 2021: The influence of ENSO on Arctic sea ice in large ensembles and observations. *J. Climate*, **34**, 9585–9604, https://doi.org/10.1175/JCLI-D-20-0958.1.

Cohen, J., and Coauthors, 2017: Recent Arctic amplification and extreme mid-latitude weather. *Nat. Geosci.*, **7**, 627–637, https://doi.org/10.1038/ngeo2234.

——, and Coauthors, 2020: Divergent consensuses on Arctic amplification influence on midlatitude severe winter weather. *Nat. Climate Change*, **10**, 20–29, https://doi.org/10.1038/s41558-019-0662-y.

Compo, G. P., and Coauthors, 2011: The Twentieth Century Reanalysis Project. *Quart. J. Roy. Meteor. Soc.*, **137** (654), 1–28, https://doi.org/10.1002/qj.776.

Dai, A., and M. Song, 2020: Little influence of Arctic amplification on mid-latitude climate. *Nat. Climate Change*, **10**, 231–237, https://doi.org/10.1038/s41558-020-0694-3.

——, D. Luo, M. Song, and J. Liu, 2019: Arctic amplification is caused by sea-ice loss under increasing CO_2. *Nat. Commun.*, **10**, 121, https://doi.org/10.1038/s41467-018-07954-9.

Ding, Q., J. M. Wallace, D. S. Battisti, E. J. Steig, A. J. E. Gallant, H.-J. Kim, and L. Geng, 2014: Tropical forcing of the recent rapid Arctic warming in northeastern Canada and Greenland. *Nature*, **509**, 209–212, https://doi.org/10.1038/nature13260.

Francis, J. A., and E. Hunter, 2006: New insight into the disappearing Arctic sea ice. *Eos, Trans. Amer. Geophys. Union*, **87**, 509–511, https://doi.org/10.1029/2006EO460001.

Fu, C., and J. Fletcher, 1985: Two patterns of equatorial warming associated with El Niño. *Chin. Sci. Bull.*, **30**, 1360–1364.

Gan, R., Q. Liu, G. Huang, K. Hu, and X. Li, 2023: Greenhouse warming and internal variability increase extreme and central Pacific El Niño frequency since 1980. *Nat. Commun.*, **14**, 394, https://doi.org/10.1038/s41467-023-36053-7.

Garfinkel, C. I., I. Weinberger, I. P. White, L. D. Oman, V. Aquila, and Y.-K. Lim, 2019: The salience of nonlinearities in the boreal winter response to ENSO: North Pacific and North America. *Climate Dyn.*, **52**, 4429–4446, https://doi.org/10.1007/s00382-018-4386-x.

Ghatak, D., and J. Miller, 2013: Implications for Arctic amplification of changes in the strength of the water vapor feedback. *J. Geophys. Res. Atmos.*, **118**, 7569–7578, https://doi.org/10.1002/jgrd.50578.

Gill, A. E., 1980: Some simple solutions for heat-induced tropical circulation. *Quart. J. Roy. Meteor. Soc.*, **106**, 447–462, https://doi.org/10.1002/qj.49710644905.

Goelzer, H., and Coauthors, 2020: The future sea-level contribution of the Greenland ice sheet: A multi-model ensemble study of ISMIP6. *Cryosphere*, **14**, 3071–3096, https://doi.org/10.5194/tc-14-3071-2020.

Graf, H.-F., and D. Zanchettin, 2012: Central Pacific El Niño, the "subtropical bridge," and Eurasian climate. *J. Geophys. Res.*, **117**, D01102, https://doi.org/10.1029/2011JD016493.

Graversen, R. G., and M. Burtu, 2016: Arctic amplification enhanced by latent energy transport of atmospheric planetary waves. *Quart. J. Roy. Meteor. Soc.*, **142**, 2046–2054, https://doi.org/10.1002/qj.2802.

——, T. Mauritsen, M. Tjernström, E. Källén, and G. Svensson, 2008: Vertical structure of recent Arctic warming. *Nature*, **451**, 53–56, https://doi.org/10.1038/nature06502.

He, S., X. Xu, T. Furevik, and Y. Gao, 2020: Eurasian cooling linked to the vertical distribution of Arctic warming. *Geophys. Res. Lett.*, **47**, e2020GL087212, https://doi.org/10.1029/2020GL087212.

Hersbach, H., and Coauthors, 2020: The ERA5 global reanalysis. *Quart. J. Roy. Meteor. Soc.*, **146**, 1999–2049, https://doi.org/10.1002/qj.3803.

Hoerling, M. P., A. Kumar, and M. Zhong, 1997: El Niño, La Niña, and the nonlinearity of their teleconnections. *J. Climate*, **10**, 1769–1786, https://doi.org/10.1175/1520-0442(1997)010<1769:ENOLNA>2.0.CO;2.

Hofer, S., C. Lang, C. Amory, C. Kittel, A. Delhasse, A. Tedstone, and X. Fettweis, 2020: Greater Greenland ice sheet contribution to global sea level rise in CMIP6. *Nat. Commun.*, **11**, 6289, https://doi.org/10.1038/s41467-020-20011-8.

Horel, J. D., and J. M. Wallace, 1981: Planetary-scale atmospheric phenomena associated with the Southern Oscillation. *Mon. Wea. Rev.*, **109**, 813–829, https://doi.org/10.1175/1520-0493(1981)109<0813:PSAPAW>2.0.CO;2.

Hoskins, B. J., I. N. James, and G. H. White, 1983: The shape, propagation and mean-flow interaction of large-scale weather systems. *J. Atmos. Sci.*, **40**, 1595–1612, https://doi.org/10.1175/1520-0469(1983)040<1595:TSPAMF>2.0.CO;2.

Hu, C., and Coauthors, 2016: Shifting El Niño inhibits summer Arctic warming and Arctic sea-ice melting over the Canada basin. *Nat. Commun.*, **7**, 11721, https://doi.org/10.1038/ncomms11721.

Huang, B., and Coauthors, 2017: Extended Reconstructed Sea Surface Temperature, version 5 (ERSSTV5): Upgrades, validations, and intercomparisons. *J. Climate*, **30**, 8179–8205, https://doi.org/10.1175/JCLI-D-16-0836.1.

Jeong, H., H. S. Park, M. F. Stuecker, and S. W. Yeh, 2022: Distinct impacts of major El Niño events on Arctic temperatures due to differences in eastern tropical Pacific sea surface temperatures. *Sci. Adv.*, **8**, eabl8278, https://doi.org/10.1126/sciadv.abl8278.

Jiménez-Esteve, B., and D. I. V. Domeisen, 2018: The tropospheric pathway of the ENSO–North Atlantic teleconnection. *J. Climate*, **31**, 4563–4584, https://doi.org/10.1175/JCLI-D-17-0716.1.

Johnson, N. C., and Y. Kosaka, 2016: The impact of eastern equatorial Pacific convection on the diversity of boreal winter El Niño teleconnection patterns. *Climate Dyn.*, **47**, 3737–3765, https://doi.org/10.1007/s00382-016-3039-1.

Jung, O., and Coauthors, 2017: How does the SST variability over the western North Atlantic Ocean control Arctic warming over the Barents–Kara Seas?. *Environ. Res. Lett.*, **12**, 034021, https://doi.org/10.1088/1748-9326/aa5f3b.

Kalnay, E., and Coauthors, 1996: The NCEP/NCAR 40-Year Reanalysis Project. *Bull. Amer. Meteor. Soc.*, **77**, 437–471, https://doi.org/10.1175/1520-0477(1996)077<0437:TNYRP>2.0.CO;2.

Kao, H.-Y., and J.-Y. Yu, 2009: Contrasting eastern-Pacific and central-Pacific types of ENSO. *J. Climate*, **22**, 615–632, https://doi.org/10.1175/2008JCLI2309.1.

Khan, S. A., and Coauthors, 2014: Sustained mass loss of the northeast Greenland Ice Sheet triggered by regional warming. *Nat. Climate Change*, **4**, 292–299, https://doi.org/10.1038/nclimate2161.

Kim, J.-Y., and K.-Y. Kim, 2019: Relative role of horizontal and vertical processes in the physical mechanism of wintertime Arctic amplification. *Climate Dyn.*, **52**, 6097–6107, https://doi.org/10.1007/s00382-018-4499-2.

Kim, K.-Y., J.-Y. Kim, J. Kim, S. Yeo, H. Na, B. D. Hamlington, and R. R. Leben, 2019: Vertical feedback mechanism of winter Arctic amplification and sea ice loss. *Sci. Rep.*, **9**, 1184, https://doi.org/10.1038/s41598-018-38109-x.

King, M. P., I. Herceg-Bulić, F. Kucharski, and N. Keenlyside, 2018: Interannual tropical Pacific sea surface temperature anomalies teleconnection to Northern Hemisphere atmosphere in November. *Climate Dyn.*, **50**, 1881–1899, https://doi.org/10.1007/s00382-017-3727-5.

Kug, J.-S., F.-F. Jin, and S.-I. An, 2009: Two types of El Niño events: Cold tongue El Niño and warm pool El Niño. *J. Climate*, **22**, 1499–1515, https://doi.org/10.1175/2008JCLI2624.1.

Larkin, N. K., 2005a: Global seasonal temperature and precipitation anomalies during El Niño autumn and winter. *Geophys. Res. Lett.*, **32**, L16705, https://doi.org/10.1029/2005GL022860.

——, 2005b: On the definition of El Niño and associated seasonal average U.S. weather anomalies. *Geophys. Res. Lett.*, **32**, L13705, https://doi.org/10.1029/2005GL022738.

Lau, N. C., and E. O. Holopainen, 1984: Transient eddy forcing of the time-mean flow as identified by geopotential tendencies. *J. Atmos. Sci.*, **41**, 313–328, https://doi.org/10.1175/1520-0469(1984)041<0313:TEFOTT>2.0.CO;2.

Lee, S., 2012: Testing of the tropically excited Arctic warming mechanism (TEAM) with traditional El Niño and La Niña. *J. Climate*, **25**, 4015–4022, https://doi.org/10.1175/JCLI-D-12-00055.1.

——, H.-S. Park, S.-Y. Song, and S.-W. Yeh, 2023: Distinct impacts of two types of El Niño events on northern winter high-latitude temperatures simulated by CMIP6 climate models. *Environ. Res. Lett.*, **18**, 034035, https://doi.org/10.1088/1748-9326/acbce9.

Li, Y., and N.-C. Lau, 2012: Impact of ENSO on the atmospheric variability over the North Atlantic in late winter—Role of transient eddies. *J. Climate*, **25**, 320–342, https://doi.org/10.1175/JCLI-D-11-00037.1.

Li, Z., W. Zhang, M. F. Stuecker, H. Xu, F.-F. Jin, and C. Liu, 2019: Different effects of two ENSO types on Arctic surface temperature in boreal winter. *J. Climate*, **32**, 4943–4961, https://doi.org/10.1175/JCLI-D-18-0761.1.

Matsumura, S., K. Yamazaki, and K. Suzuki, 2021: Slow-down in summer warming over Greenland in the past decade linked to central Pacific El Niño. *Commun. Earth Environ.*, **2**, 257, https://doi.org/10.1038/s43247-021-00329-x.

McCrystall, M. R., J. S. Hosking, I. P. White, and A. C. Maycock, 2020: The impact of changes in tropical sea surface temperatures over 1979–2012 on Northern Hemisphere high-latitude climate. *J. Climate*, **33**, 5103–5121, https://doi.org/10.1175/JCLI-D-19-0456.1.

Meyssignac, B., X. Fettweis, R. Chevrier, and G. Spada, 2017: Regional sea level changes for the twentieth and the twenty-first centuries induced by the regional variability in Greenland ice sheet surface mass loss. *J. Climate*, **30**, 2011–2028, https://doi.org/10.1175/JCLI-D-16-0337.1.

Park, H.-S., S. Lee, S.-W. Son, S. B. Feldstein, and Y. Kosaka, 2015: The impact of poleward moisture and sensible heat flux on Arctic winter sea ice variability. *J. Climate*, **28**, 5030–5040, https://doi.org/10.1175/JCLI-D-15-0074.1.

Park, K., S. M. Kang, D. Kim, M. F. Stuecker, and F. F. Jin, 2018: Contrasting local and remote impacts of surface heating on polar warming and amplification. *J. Climate*, **31**, 3155–3166, https://doi.org/10.1175/JCLI-D-17-0600.1.

Rantanen, M., A. Y. Karpechko, A. Lipponen, K. Nordling, O. Hyvärinen, K. Ruosteenoja, T. Vihma, and A. Laaksonen, 2022: The Arctic has warmed nearly four times faster than the globe since 1979. *Commun. Earth Environ.*, **3**, 168, https://doi.org/10.1038/s43247-022-00498-3.

Rasmusson, E. M., and T. H. Carpenter, 1982: Variations in tropical sea surface temperature and surface wind fields associated with the Southern Oscillation/El Niño. *Mon. Wea. Rev.*, **110**, 354–384, https://doi.org/10.1175/1520-0493(1982)110<0354:VITSST>2.0.CO;2.

Roeckner, E., and Coauthors, 2003: The atmospheric general circulation model ECHAM 5. Part I: Model description. Max Planck Institute for Meteorology Rep. 349, 127 pp., https://hdl.handle.net/11858/00-001M-0000-0012-0144-5.

Screen, J. A., and I. Simmonds, 2010: The central role of diminishing sea ice in recent Arctic temperature amplification. *Nature*, **464**, 1334–1337, https://doi.org/10.1038/nature09051.

——, C. Deser, and I. Simmonds, 2012: Local and remote controls on observed Arctic warming. *Geophys. Res. Lett.*, **39**, L10709, https://doi.org/10.1029/2012GL051598.

——, and Coauthors, 2018: Consistency and discrepancy in the atmospheric response to Arctic sea-ice loss across climate models. *Nat. Geosci.*, **11**, 155–163, https://doi.org/10.1038/s41561-018-0059-y.

Serreze, M. C., A. P. Barrett, and J. Stroeve, 2012: Recent changes in tropospheric water vapor over the Arctic as assessed from radiosondes and atmospheric reanalyses. *J. Geophys. Res.*, **117**, D10104, https://doi.org/10.1029/2011JD017421.

Shepherd, A., and Coauthors, 2020: Mass balance of the Greenland ice sheet from 1992 to 2018. *Nature*, **579**, 233–239, https://doi.org/10.1038/s41586-019-1855-2.

Stuecker, M. F., and Coauthors, 2018: Polar amplification dominated by local forcing and feedbacks. *Nat. Climate Change*, **8**, 1076–1081, https://doi.org/10.1038/s41558-018-0339-y.

Takahashi, K., A. Montecinos, K. Goubanova, and B. Dewitte, 2011: ENSO regimes: Reinterpreting the canonical and Modoki El Niño. *Geophys. Res. Lett.*, **38**, L10704, https://doi.org/10.1029/2011GL047364.

Takaya, K., and H. Nakamura, 2001: A formulation of a phase-independent wave-activity flux for stationary and migratory quasigeostrophic eddies on a zonally varying basic flow. *J. Atmos. Sci.*, **58**, 608–627, https://doi.org/10.1175/1520-0469(2001)058<0608:AFOAPI>2.0.CO;2.

Trenberth, K. E., 1986: An assessment of the impact of transient eddies on the zonal flow during a blocking episode using localized Eliassen-Palm flux diagnostics. *J. Atmos. Sci.*, **43**, 2070–2087, https://doi.org/10.1175/1520-0469(1986)043<2070:AAOTIO>2.0.CO;2.

——, 1997: The definition of El Niño. *Bull. Amer. Meteor. Soc.*, **78**, 2771–2778, https://doi.org/10.1175/1520-0477(1997)078<2771:TDOENO>2.0.CO;2.

——, G. W. Branstator, D. Karoly, A. Kumar, N.-C. Lau, and C. Ropelewski, 1998: Progress during TOGA in understanding and modeling global teleconnections associated with tropical sea surface temperatures. *J. Geophys. Res.*, **103**, 14 291–14 324, https://doi.org/10.1029/97JC01444.

Vallis, G. K., 2017: *Atmospheric and Oceanic Fluid Dynamics.* Cambridge University Press, 946 pp.

Vargas Zeppetello, L. R., A. Donohoe, and D. S. Battisti, 2019: Does surface temperature respond to or determine downwelling longwave radiation? *Geophys. Res. Lett.*, **46**, 2781–2789, https://doi.org/10.1029/2019GL082220.

Wang, B., and Coauthors, 2019: Historical change of El Niño properties sheds light on future changes of extreme El Niño. *Proc. Natl. Acad. Sci. USA*, **116**, 22 512–22 517, https://doi.org/10.1073/pnas.1911130116.

Weijer, W., M. E. Maltrud, M. W. Hecht, H. A. Dijkstra, and M. A. Kliphuis, 2012: Response of the Atlantic Ocean circulation to Greenland ice sheet melting in a strongly-eddying ocean model. *Geophys. Res. Lett.*, **39**, L09606, https://doi.org/10.1029/2012GL051611.

Yang, Y. M., J. H. Park, S. I. An, B. Wang, and X. Luo, 2021: Mean sea surface temperature changes influence ENSO-related precipitation changes in the mid-latitudes. *Nat. Commun.*, **12**, 1495, https://doi.org/10.1038/s41467-021-21787-z.

Yeh, S. W., J. S. Kug, B. Dewitte, M. H. Kwon, B. P. Kirtman, and F. F. Jin, 2009: El Niño in a changing climate. *Nature*, **461**, 511–514, https://doi.org/10.1038/nature08316.

Yoshimori, M., A. Abe-Ouchi, and A. Laîné, 2017: The role of atmospheric heat transport and regional feedbacks in the Arctic warming at equilibrium. *Climate Dyn.*, **49**, 3457–3472, https://doi.org/10.1007/s00382-017-3523-2.